

Evolution of helium bubbles in FeCoNiCr-based high-entropy alloys containing γ' nanoprecipitates

Ting Feng(冯婷), Sheng-Ming Jiang(蒋胜明), Xiao-Tian Hu(胡潇天), Zi-Jun Zhang(张子骏), Zi-Jing Huang(黄子敬), Shi-Gang Dong(董士刚), and Jian Zhang(张建)

Citation: Chin. Phys. B, 2024, 33 (**7**): 076501. DOI: 10.1088/1674-1056/ad342f
Journal homepage: http://cpb.iphy.ac.cn; http://iopscience.iop.org/cpb

What follows is a list of articles you may be interested in

Enhanced superelasticity and reversible elastocaloric effect in nano-grained NiTi alloys with low stress hysteresis

Min Zhou(周敏), Wei Wang(王维), Haojian Su(苏浩健), Zhongjun Hu(胡忠军), and Laifeng Li(李来风)
Chin. Phys. B, 2024, 33 (**5**): 056501. DOI: 10.1088/1674-1056/ad2a75

Microstructure and hardening effect of pure tungsten and ZrO_2 strengthened tungsten under carbon ion irradiation at 700℃

Chun-Yang Luo(罗春阳), Bo Cui(崔博), Liu-Jie Xu(徐流杰), Le Zong(宗乐), Chuan Xu(徐川), En-Gang Fu(付恩刚), Xiao-Song Zhou(周晓松), Xing-Gui Long(龙兴贵), Shu-Ming Peng(彭述明), Shi-Zhong Wei(魏世忠), and Hua-Hai Shen(申华海)
Chin. Phys. B, 2022, 31 (**9**): 096102. DOI: 10.1088/1674-1056/ac6b25

Helium bubble formation and evolution in NiMo-Y_2O_3 alloy under He ion irradiation

Awen Liu(刘阿文), Hefei Huang(黄鹤飞), Jizhao Liu(刘继召), Zhenbo Zhu(朱振博), and Yan Li(李燕)
Chin. Phys. B, 2022, 31 (**4**): 046102. DOI: 10.1088/1674-1056/ac3654

Effect of tellurium (Te^{4+}) irradiation on microstructure and associated irradiation-induced hardening

Hefei Huang(黄鹤飞), Jizhao Liu(刘继召), Guanhong Lei(雷冠虹), Ondrej Muránsky, Tao Wei, and Mihail Ionescu
Chin. Phys. B, 2021, 30 (**5**): 056108. DOI: 10.1088/1674-1056/abf039

Elastocaloric effect and mechanical behavior for NiTi shape memory alloys

Min Zhou(周敏), Yu-Shuang Li(李玉霜), Chen Zhang(张晨), Lai-Feng Li(李来风)
Chin. Phys. B, 2018, 27 (**10**): 106501. DOI: 10.1088/1674-1056/27/10/106501

Evolution of helium bubbles in FeCoNiCr-based high-entropy alloys containing γ' nanoprecipitates

Ting Feng(冯婷), Sheng-Ming Jiang(蒋胜明), Xiao-Tian Hu(胡潇天), Zi-Jun Zhang(张子骏), Zi-Jing Huang(黄子敬), Shi-Gang Dong(董士刚), and Jian Zhang(张建)†

College of Energy, Xiamen University, Xiamen 361005, *China*

(Received 23 January 2024; revised manuscript received 8 March 2024; accepted manuscript online 15 March 2024)

A series of high-entropy alloys (HEAs) containing nanoprecipitates of varying sizes is successfully prepared by a non-consuming vacuum arc melting method. In order to study the irradiation evolution of helium bubbles in the FeCoNiCr-based HEAs with γ' precipitates, these samples are irradiated by 100-keV helium ions with a fluence of 5×10^{20} ions/m^2 at 293 K and 673 K, respectively. And the samples irradiated at room temperature are annealed at different temperatures to examine the diffusion behavior of helium bubbles. Transmission electron microscope (TEM) is employed to characterize the structural morphology of precipitated nanoparticles and the evolution of helium bubbles. Experimental results reveal that nanosized, spherical, dispersed, coherent, and ordered $L1_2$-type Ni_3Ti γ' precipitations are introduced into FeCoNiCr$(Ni_3Ti)_{0.1}$ HEAs by means of ageing treatments at temperatures between 1073 K and 1123 K. Under the ageing treatment conditions adopted in this work, γ' nanoparticles are precipitated in FeCoNiCr$(Ni_3Ti)_{0.1}$ HEAs, with average diameters of 15.80 nm, 37.09 nm, and 62.50 nm, respectively. The average sizes of helium bubbles observed in samples after 673-K irradiation are 1.46 nm, 1.65 nm, and 1.58 nm, respectively. The improvement in the irradiation resistance of FeCoNiCr$(Ni_3Ti)_{0.1}$ HEAs is evidenced by the diminution in bubbles size. Furthermore, the FeCoNiCr$(Ni_3Ti)_{0.1}$ HEAs containing γ' precipitates of 15.8 nm exhibits the minimum size and density of helium bubbles, which can be ascribed to the considerable helium trapping effects of heterogeneous coherent phase boundaries. Subsequently, annealing experiments conducted after 293-K irradiation indicate that HEAs containing precipitated phases exhibits smaller apparent activation energy (E_a) for helium bubbles, resulting in larger helium bubble size. This study provides guidance for improving the irradiation resistance of $L1_2$-strengthened high-entropy alloy.

Keywords: high-entropy alloys, irradiation resistance, coherent precipitates, helium bubbles

PACS: 65.40.gd, 61.80.Lj, 47.27.De, 61.66.Dk **DOI:** 10.1088/1674-1056/ad342f

1. Introduction

The development of the nuclear industry has put forward higher requirements for the performance of advanced nuclear reactor materials. The operating environment of reactors is challenging, and the materials applicated to it will encounter extreme conditions, including high-dose radiation, high temperatures, and a corrosive atmosphere.[1–3] Such conditions inevitably result in significant deterioration or even complete failure of material properties and structural performance.[4–7] As such, the search for structural materials that can withstand harsh circumstances is imperative for prolonging the lifespan of reactors and the development of proposed fusion and advanced fission reactors. Neutron irradiation is known to introduce transmutation elements such as hydrogen and helium, which can cause damage to their crystalline structure and ultimately shorten the service lifespan. Helium could agglomerate into detrimental helium bubbles due to its extremely low solubility in alloys, leading to severe volume swelling and irradiation embrittlement.[8,9] This is one of the most critical problems that needs solving for future development of advanced structural materials.

High-entropy alloy (HEA) is composed of many principal elements, which has unique constituent design, adjustable microstructure and excellent mechanical properties, showing high hardness, high wear resistance and corrosion resistance, excellent strength and high oxidation resistance, and has been widely concerned in recent years.[10,11] Some investigations suggest that high-entropy alloys also perform better irradiation resistance than conventional superalloys.[12,13] As demonstrated in Ni-based alloys by Lu *et al.*,[14] concentrated solid solution alloys, including NiFe, NiCoFe, NiCoCrFe, and NiCoCrFeMn, were irradiated by 3-MeV Ni^{2+} with a total fluence of 5×10^{20} ions/m^2 at 773 K. The results revealed that smaller dislocation loops exist in high-entropy alloys, suggesting that greater compositional complexity can effectively delay loops growth.

The single-phase face-centered cubic (FCC) high-entropy alloys have demonstrated superior mechanical properties,[15] there is still room for improvement in strength. The $L1_2$-strengthened dual-phase high-entropy alloys can enhance hardness without sacrificing ductility, thereby achieving the desired trade-off between strength and ductility. Therefore, the incorporatio of γ' nanoparticles, as a novel approach in designing structural materials, has great potential in achieving a superior strength-ductility combination. The authors in

†Corresponding author. E-mail: zhangjian@xmu.edu.cn

© 2024 Chinese Physical Society and IOP Publishing Ltd

Ref. [16] discovered that coarse-grained high-entropy alloys $Al_{0.2}Co_{1.5}FeCrNi_{1.5}Ti_{0.3}$ alloys display both a yield strength of 750 MPa and ultimate tensile strength of 1160 MPa. However, elongation to fracture decreases from 42% to 12% with aging time increasing from 1 h to 100 h. The introduction of high-density defect sinks has been presented as a promising strategy for improving radiation resistance associated with alleviating the accumulation of radiation-induced damage.[17,18] Zheng *et al.* studied the CoCrFeNi single-phase alloy and $(CoCrFeNi)_{94}Ti_2Al_4$ dual-phase alloy irradiated by 2.7-MeV Fe^{11+} at 823 K.[19] The size of dislocation loops in $(CoCrFeNi)_{94}Ti_2Al_4$ was significantly reduced due to the presence of γ' coherent nanoprecipitates. The $L1_2$-type γ' nanoparticles can be used as effective defect sinks to reduce structural damage, thus improving irradiation tolerance.[20]

Helium bubbles are observed as the primary irradiation damage in $L1_2$-strengthened HEAs irradiated under He^+ irradiation.[21–23] Helium bubbles, which are typical defects caused by irradiation, can result in helium embrittlement, volume swelling, and other negative effects that significantly degrade industry properties.[5,24] Therefore, the irradiation response of the material needs further improving by suppressing the helium bubble evolution behavior. FeCoNiCr-based high-entropy alloys with excellent mechanical properties have been proposed as favorable competitor of structural materials for the next generation of reactors.[25] Recently, it has been generally believed that the high-density secondary phase strengthening in materials (whether semi-coherent or non-coherent) can enhance radiation resistance by promoting the recombination of defects at the interface.[26–28] A combined TEM and APT characterization shows that the bubble size decreases in the $L1_2$-strengthened HEAs compared with that in the single-phase FeCoNiCr HEAs. This indicates that the $L1_2$ nanoprecipitates can prevent bubble from growing, thus improving an enhanced radiation resistance.[29] However, further research is required to determine the influence of coherent interfaces on enhancing irradiation resistance.

In this study, γ' precipitates with diameters of 15.80 ± 1.96 nm, 37.09 ± 3.08 nm, and 62.50 ± 10.10 nm are introduced into FeCoNiCr-based high-entropy alloys through ageing treatments. The $L1_2$-strengthened HEAs with a nominal composition of $FeCoNiCr(Ni_3Ti)_{0.1}$ (at.%) are then subjected to 100-keV helium ions irradiation at 293 K and 673 K. The study systematically analyzes the behavior of helium bubbles to ascertain the considerable helium trapping effects of coherent phase boundaries in detail.

2. Experimental procedures

2.1. Samples preparation

The alloy ingots with a nominal composition of $FeCoNiCr(Ni_3Ti)_{0.1}$ (atomic percentage) were fabricated by using a non-consumable vacuum arc-melting furnace in this study. Iron, cobalt, nickel, chromium, and titanium particles, with a purity of 99.99%, were accurately weighed and consequently melted in a water-cooled copper crucible within a Ti-getter argon atmosphere. Fully melted ingots were stirred 5–8 times to achieve uniform alloy composition. As-cast bulk alloys were solid solution treated at 1423 K for 5 h in an Ar atmosphere tube furnace with Ar atmosphere to achieve homogenization.

After the aforementioned solid solution treatments, samples with consistent grain structure were then aged at various temperatures to introduce nanoprecipitates. Specifically, specimens were subjected to ageing treatments at 1073 K for 5 hours, 1123 K for 10 hours, and 1123 K for 50 hours, and they were denoted as HEA-16, HEA-37, and HEA-63, respectively. All heat treatments were followed by the water quenching.

The samples were cut into the thin slices each with size 5 mm×5 mm×1 mm by using a wire-electrode, and then mechanically polished to ∼60 μm in thickness by using 2000-grit SiC papers. Unirradiated specimens were prepared through an electrochemical etching method with dual-jet electrolyte of 10% perchloric acid and 90% ethanol by volume fraction at −30 °C and 30 V. Cross-sectional samples after irradiation were precisely thinned with 5-keV Ar^+ incident at 5° by the precision ion polishing system (PIPS, Gatan) for TEM observation. Irradiation is typically performed on single crystals without considering the influence of grain boundaries. Due to the large grain size of hundreds of micrometers, the influence of grain boundaries is eliminated from the irradiation response.

2.2. He^+ irradiation

Helium ion irradiation were performed at the Xiamen University Multiple Ion Beam *In-situ* TEM Analysis Facility.[30] The specimens were well-polished and then irradiated with 100-keV helium ions, respectively, at 293 K and 673 K, with a total fluence of 5×10^{20} ions/m^2. The Stopping and Range of Ions in Matter (SRIM-2013) program utilized the quick Kinchin–Pease mode to predict damage profiles and helium concentration. The displacement threshold energy, E_d, was set to be 25 eV for all elements. By keeping the energy and dose for all implanted ions equal, the displacement and helium concentration distribution among all studied materials predicted by SRIM are comparable to each other.

2.3. TEM characterization

The Tecnai F30 transmission electron microscope (TEM) operating with an acceleration voltage of 300 kV was carefully employed to investigate the microstructural features of nanoprecipitates. Energy-dispersive x-ray spectroscopy (EDS) was carried out to characterize the elemental distribution of both

matrices and precipitates. The images of helium bubbles were taken with through-focus, in which the helium bubbles underfocus present as white owing to Fresnel contrast.[31]

3. Results

3.1. The γ' precipitates

The XRD patterns of unirradiated samples are shown in Fig. 1. It can be seen that all four samples are face-centered cubic (FCC) structures before irradiation, where peaks occurring at $2\theta = 43.6°$, $50.8°$, and $75.0°$ correspond to (111), (200), and (220) lattice planes of FCC. Both the γ phase and γ' phase have an FCC structure, are highly coherent, and have similar lattice constants. Therefore, the peaks of γ and γ' exhibited on the XRD patterns are closely overlapped in Fig. 1 (corresponding to PDF card# 47-1405 and PDF card# 09-0097). It is evident that the unirradiated quinary FeCoNiCr$(Ni_3Ti)_{0.1}$ HEAs contain no impurity phases according to Fig. 1.

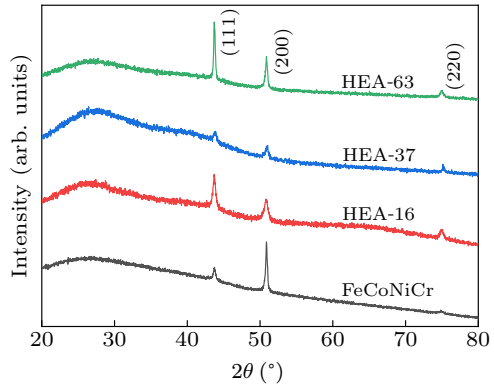


Fig. 1. XRD patterns of unirradiated FeCoNiCr, HEA-16, HEA-37, and HEA-63 samples.

In addition, the peak position of FCC shifts to the left slightly due to the addition of the Ti element. This phenomenon can be attributed to the significant swelling of the lattice due to the presence of large-sized Ti atoms, resulting in an increase in the lattice constant. There is a noticeable hump peak at $2\theta = 20°$–$30°$, which is due to the fact that the x-ray diffractometer we used is a Cu target, and the fluorescence spectra from the sample containing ferromagnetic elements cannot be completely eliminated. And typical iron can be measured by using cobalt radiation to prevent fluorescence.[32]

Previous research conducted by our group revealed that FeCoNiCr alloy possesses a homogenous single-phase composition,[33] consequently we shall not reiterate those findings here. The TEM images as shown in Fig. 2 validate the morphologies and distributions of the γ' nanoprecipitates. The scale bar varies with particle size. Evidently, high-density, uniformity, dispersion of spherical nanoparticles are observed in the unirradiated FeCoNiCr$(Ni_3Ti)_{0.1}$ HEA. The statistical results indicate that the average sizes of the precipitates are 15.80 ± 1.96 nm, 37.09 ± 3.08 nm, and 62.50 ± 10.10 nm in the samples, and in the following, the sample will be named HEA-16, HEA-37, and HEA-63, respectively. The illustrations depict the selected electron diffraction patterns (SAED) taken along the [001] zone axis, as can be seen in the inset of corresponding BF TEM image. The white arrows mark the superlattice spots of γ'. The EDS map scanning and line scanning profiles are shown in Fig. 3, demonstrate element distributions within the precipitate and matrix. The map scanning in Fig. 3(a) displays overall elements' distribution of HEA-16, revealing an enriched concentration of Ni and Ti atoms, while Fe, Co, and Cr atoms are relatively uniform distribution. The positions of the EDS line scanning are determined based on the morphology and elements of the precipitated phases in the STEM images. And the line scanning in Fig. 3(b) exhibits the result of HEA-63, which indicates an evident increase in Ni and Ti content nearby the γ' nanoparticle. The composition profiles *versus* precipitate demonstrate the precipitation of Ni_3Ti with stoichiometric proportions. The elemental scanning of HEA-37 presents similar results so they are omitted here. Therefore it can be concluded that γ' precipitations of all FeCoNiCr$(Ni_3Ti)_{0.1}$ HEAs are embedded in γ matrices with the $L1_2$-type of Ni_3Ti stoichiometry. Additionally, the bright lines are dislocation lines contained in the original samples. The distortion of the crystal atomic arrangement at the dislocations is represented by the contrast in the STEM image.

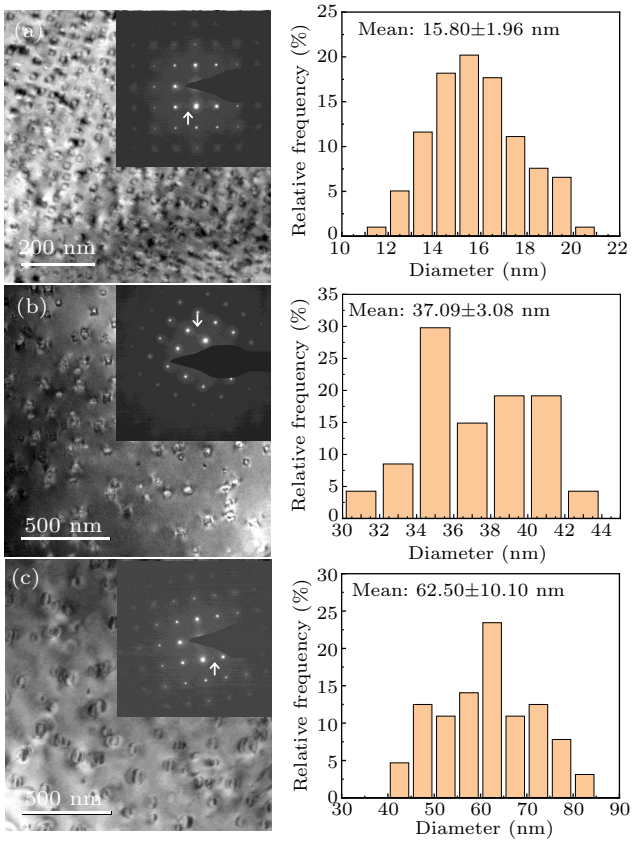


Fig. 2. Bright-field TEM images of high-entropy alloys after aging treatments. (a)–(c) BF-TEM images of HEA-16, HEA-37, and HEA-63 with corresponding SAEDs along [001] zone axis, with white arrows indicating the presence of superlattice spots. Average size statistics of the precipitates in each sample are shown on the right, which are 15.80 ± 1.96 nm, 37.09 ± 3.08 nm, and 62.50 ± 10.10 nm, respectively.

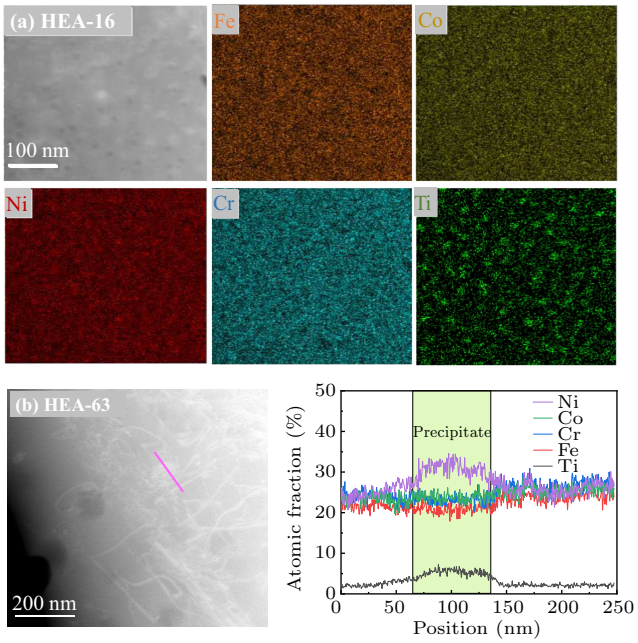


Fig. 3. EDS results of HEA-16 and HEA-63. (a) EDS mapping of HEA-16, where Ni and Ti atoms are enriched. (b) Line scanning of HEA-63 showing that Ni content and Ti content increase evidently nearby the precipitate.

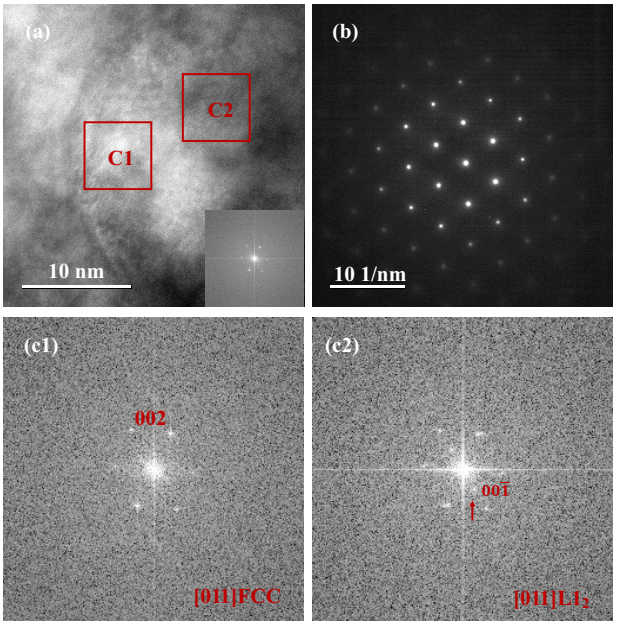


Fig. 4. High-resolution TEM (HRTEM) image of HEA-16, showing (a) matrix region C1 and precipitated phase region C2 and (b) SAED pattern under [011] zone axis.

The HRTEM images of the HEA-16 sample under the [011] zone axis of γ' ordered precipitates in matrix are shown in Fig. 4. The images in Figs. 4(c1) and 4(c2) are FFT patterns of regions C1 and C2 in Fig. 4(a), respectively, from which the superlattice spots of γ' ordered precipitates can be clearly seen. The lattice constants of the γ' precipitated and γ matrix were accurately measured from the high-resolution TEM image. The lattice constants of γ' and γ are 0.3559 nm and 0.3562 nm, respectively. As a result, the lattice misfit of γ' and γ are estimated to be about 0.084%, which indicates a strong coherence between the phases γ and γ'. Conclusively, the ordered γ' phases display a high level of coherence with the FCC matrix. Figure 4(b) shows the SAED image, and the region chosen by the selected aperture contains a significant number of matrices, which may mask the superlattice spot signals of the precipitated phase under the [011] zone axis. Additionally, the superlattice spots may not be visible due to the sample's thickness and the limited ordering of the precipitated γ' phases. However, the fast Fourier transform (FFT) of the high-resolution TEM reveals the corresponding superlattice spots as shown in the inset of Fig. 4(a), which is due to the fact that the micro-region is observed in high-resolution TEM mode, and allows for the visualization of the superlattice spots.

3.2. The 673-K He^+ irradiation

To evaluate the irradiation resistances of high-entropy alloys containing coherent precipitations, well-polished bulk samples were exposed to 100-keV helium ions with a fluence of 5×10^{20} ions/m^2 at 673 K. Figure 5 reveals corresponding simulation of the SRIM procedure, along with panoramic cross-sectional images. Since the energy values of helium ions are identical (100 keV) across all four similar composition samples, their SRIM graphs show no meaningful variation, and thus only one graph is displayed here. The ion irradiation incidence direction is perpendicular to the surface. It can be seen that the irradiation depth is approximately 500 nm, and the damage dose approaches a peak value of $\sim$ 2.2 dpa at $\sim$ 300 nm and the peak helium concentration reaches $\sim$ 3 at.% at $\sim$ 350 nm. The two characteristic regions are the low (1 at.%) and peak (3 at.%) helium concentration regions, where the average sizes and densities of bubbles are calculated statistically. Cross-sectional images show the presence of numerous defect clusters induced by the ion irradiation, which are densely distributed in a depth range of 250 nm–350 nm. This depth range agrees well with the peak damage region that is predicted by SRIM.

The distributions of helium bubbles in the helium concentration peak regions taken by through-focus are shown in Fig. 6. A higher density of small, mutually isolated helium bubbles at a nanoscale level is visible in each of the BF-TEM images, which appears as white dots with black streaks in the under-focused mode and black dots with white streaks in the over-focused mode within irradiated HEAs. The scale bar and defocus value are standardized during taking images. The average sizes of helium bubbles in irradiated FeCoNiCr, HEA-16, HEA-37, and HEA-63 are shown on the right, which are 2.02 ± 0.40 nm, 1.46 ± 0.21 nm, 1.65 ± 0.32 nm, and 1.58 ± 0.32 nm, respectively. The images in the third column of the figure are the enlarged images in the first column on the left, from which it can be seen very clearly that the size and density of the helium bubbles in sample HEA-16 are the smallest.

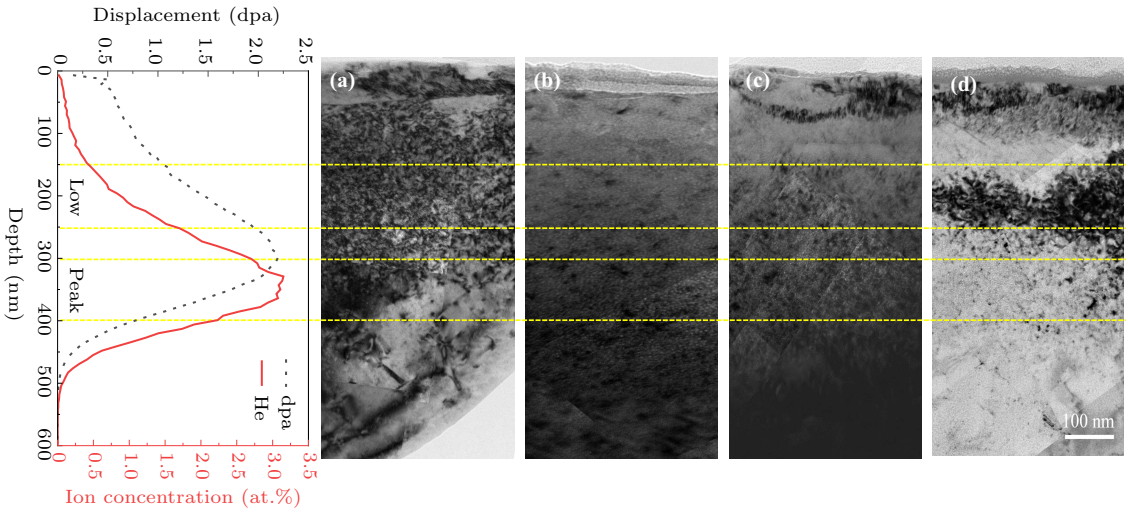


Fig. 5. SRIM calculation results of corresponding irradiation damage and He concentration plotted as a function of depth for (a)–(d) are cross-sectional specimens of (a) FeCoNiCr, (b) HEA-16, (c) HEA-37, and (d) HEA-63 irradiated by 100-keV He ions at 673 K, respectively.

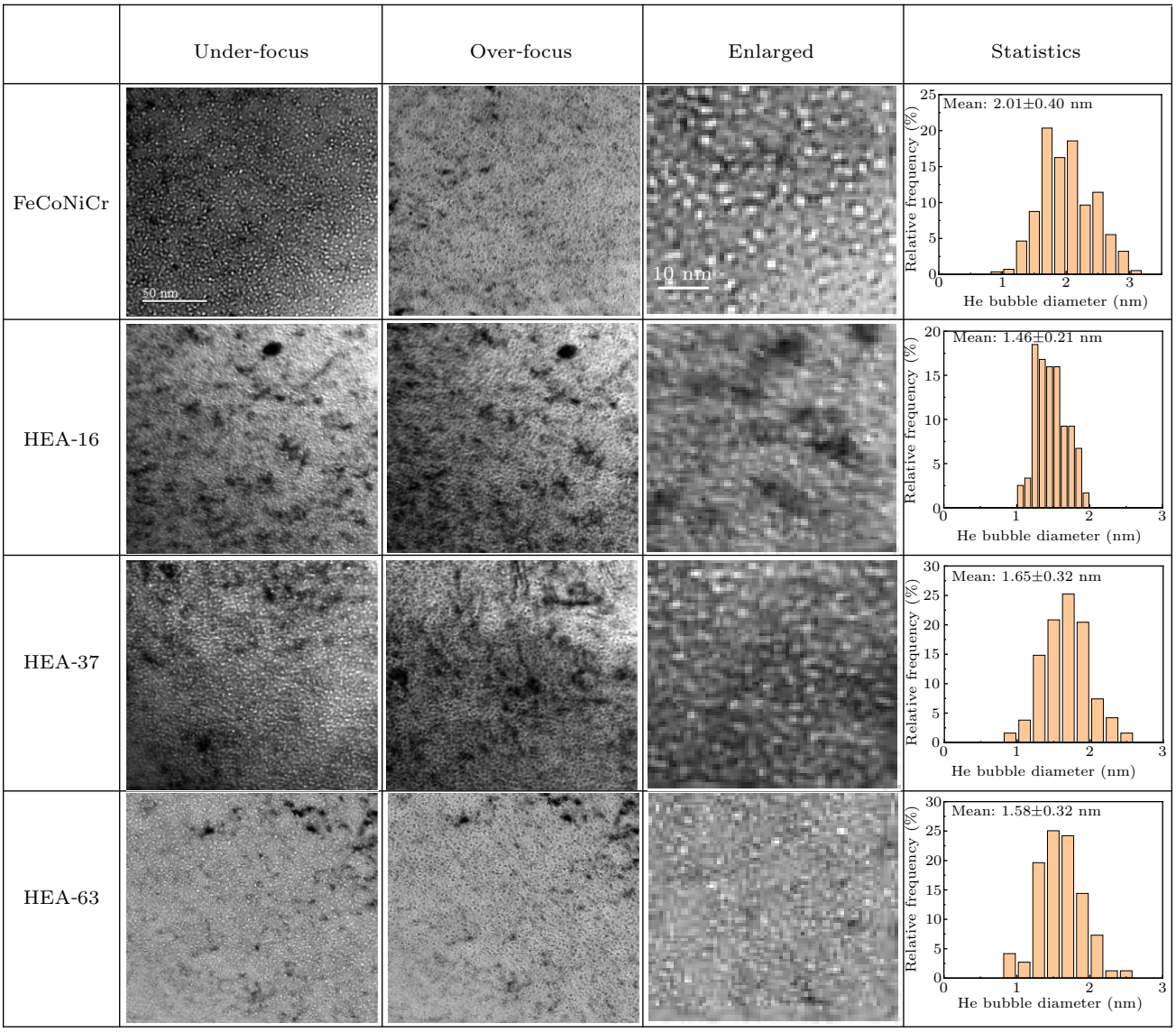


Fig. 6. Micrographs of helium bubbles taken from He concentration peak regions of FeCoNiCr, HEA-16, HEA-37, and HEA-63 under under-focus and over-focus conditions, and average size statistics of He bubbles in each sample shown on the right, which are 2.02 ± 0.40 nm, 1.46 ± 0.21 nm, 1.65 ± 0.32 nm, and 1.58 ± 0.32 nm, respectively. The third column displays corresponding enlargement of the first column. All micrographs have the same magnification.

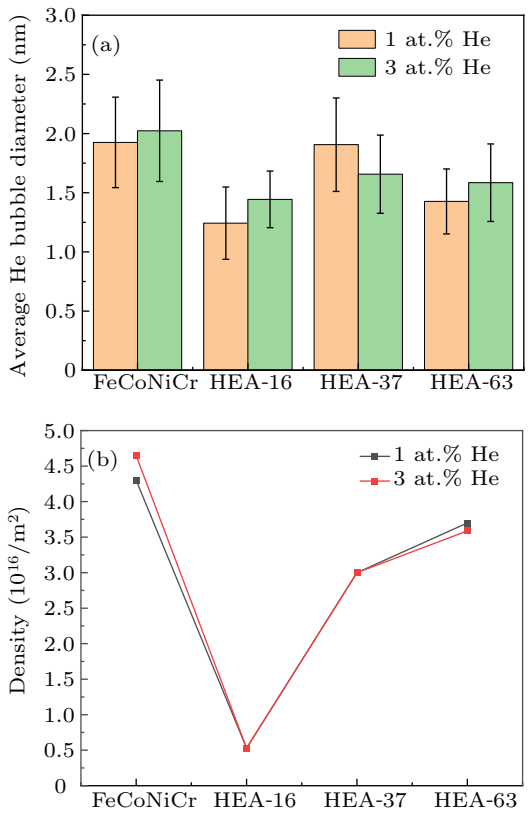


Fig. 7. (a) Average sizes and (b) density of helium bubbles in two regions of FeCoNiCr, HEA-16, HEA-37, and HEA-63.

Further statistical analysis reveals the evolution of helium bubbles in two characteristic regions as shown in Fig. 7. These regions have different helium concentrations, which are marked by yellow dotted lines in Fig. 5. The size distribution of bubbles is statistically analyzed for at least three images of the same depth, with a minimum value of 800-helium bubbles counted in each region for the reliability of results. Results indicate that the FeCoNiCr alloy possesses the largest helium bubble size of approximately 2 nm, whereas HEA-16 containing 15.8-nm γ' precipitates has the smallest size of less than 1.5 nm. The average size of He bubbles in HEA-37 and HEA-63 are roughly comparable: they are measured to be about 1.7 nm and 1.6 nm, respectively. Based on the statistical evidence as shown in Fig. 7(b), HEA-16 displays the smallest helium bubble density, specifically, 0.5×10^{16} m^{-2}, whereas the largest helium bubble density can be found in the FeCoNiCr alloy, which is roughly 9 times greater than that of HEA-16 as shown in Table 1. Additionally, helium bubble density in HEA-37 and HEA-63 are similar. Statistical value of helium bubble average diameters and distribution densities in Fig. 7 are approximately equal at 1-at.% and 3-at.% helium concentrations, which may be due to the fact that helium atoms reach a saturation concentration.[29,34] It is worth noting that the TEM observation sample of HEA-16 in Fig. 7 is prepared by the focused ion beam (FIB) method, which has a relatively uniform thickness of 100 nm. This leads to the conclusion that high-entropy alloys containing high-density coherent nanoprecipitates exhibit superior radiation resistance. It is counter-intuitive that different HEAs show the same trend for densities and sizes of helium bubbles in this experiment. That is to say, helium bubbles in HEA-16 with the smallest size and also have the lowest density simultaneously. Further analysis of this phenomenon is presented in detail in the following subsection.

Table 1. Relative diameters and densities of He bubbles in irradiated HEAs containing different values of size γ' at 673 K, with R_L and R_P denoting diameters of He bubbles in low He concentration region and peak He concentration region, and C_L and C_P representing densities of He bubbles in low He concentration region and peak He concentration region.

γ' size (nm)	R_L (nm)	R_P (nm)	C_L (10^{16}/m^2)	C_P (10^{16}/m^2)
–	1.85	2.02	4.25	4.60
15.80	1.25	1.46	0.50	0.50
37.09	1.82	1.65	3.00	3.00
62.50	1.46	1.58	3.52	3.48

3.3. The 293-K He$^+$ irradiation

To investigate the irradiation resistance mechanism of high-entropy alloys, annealing experiments are carried out after the bulk samples have been irradiated by 100-keV helium ions with a fluence of 5×10^{20} ions/m^2 at 293 K. In detail, samples FeCoNiCr and HEA-63 are held at 523 K, 623 K, and 723 K for 10 min sequentially, while sample HEA-16 is held at 473 K and 673 K for 30 min. The heating time and cooling time during the experiments are both within 4 min. Additionally, the temperatures are lowered to room temperature before transmission electron microscopy observations are made. Figures 8(a)–8(c) display the cross-sectional TEM images of FeCoNiCr, HEA-16, and HEA-63 after ex-irradiation at 293 K. A distinct boundary between the irradiated layer and the substrate is visible, which is consistent with the results of

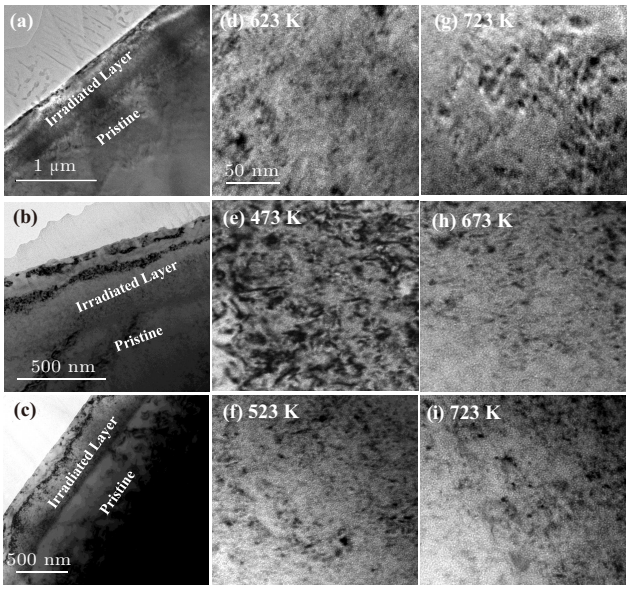


Fig. 8. Cross-sectional TEM images of (a) FeCoNiCr, (b) HEA-16, and (c) HEA-63 at 293 K and peak helium concentration regions in FeCoNiCr at (d) 623 K, (g) 723 K, HEA-16 at (e) 473 K and (h) 673 K, and HEA-63 at (f) 523 K and (i) 723 K, with (d)–(i) panels sharing the same scale bar.

the SRIM simulations and indicates an irradiation depth of approximately 500 nm. Figures 8(d), 8(g), 8(e), 8(h), 8(f), and 8(i) show the peak helium concentration regions in FeCoNiCr at 623 K and 723 K, HEA-16 at 473 K and 673 K, HEA-63 at 523 K and 723 K, respectively. It is evident that the size of the helium bubble is the largest in sample HEA-16 and the smallest in FeCoNiCr. Specific statistics are available in Fig. 9, and this observation is contrary to the results obtained from He^+ irradiation at 673 K. Further discussion will be conducted in Subsection 4.3.

4. Discussion

4.1. Helium diffusion

Due to the extremely low solubility and high migration rate of helium in metals,[35] helium atoms exist primarily in the form of interstitial helium (He_i) or substituted helium (He_s) in crystalline particles. To clarify, He_i refers to helium that is located in an interstitial site, while He_s denotes helium occupying the substitutional site. Under the experimental conditions, it can be determined that both monovacancy (V) and He_i act as mobile defects. Binary reactions outlined in the following produce a significant number of defect complex clusters:

$$He_i + V \rightleftharpoons HeV, \tag{1}$$

$$HeV + I \rightleftharpoons He_i. \tag{2}$$

According to Li *et al.*,[7] He_s replaces He_i via the Frank–Turnbull dissociative reaction involving vacancies (reaction (1)), or perhaps associated with the kick-out reaction involving self-interstitials (I) (reaction (2)). Furthermore, He_s and He_i, which can spontaneously replace each other, enable the movement of He_i atoms after transformation from He_s. Helium continues to diffuse, incubate, nucleate and finally evolves into a thermally stable helium bubble according to above reactions. Helium atom gradually agglomerates into a large-sized helium bubble, causing harmful problems such as irradiation swelling and helium embrittlement.[3] Additionally, point defects caused by cascade collisions play an important role in the evolution process of helium bubbles. After a helium bubble nucleates, the absorption of both vacancy and helium atoms promotes the growth of the bubble.[36] The addition of self-interstitial atoms (SIAs) conversely causes the helium bubbles to shrink. In the radiation experiment with helium atoms injected, the evolution of helium bubbles, including density and size, is primarily determined by temperature, irradiation dose, displacement rate, and helium production rate.[35] In line with that, this phenomenon can be seen evidently that the helium bubbles in the panorama (Fig. 5) are concentrated in the peak range of helium concentration and the helium productivity is correspondingly high in this range.

During helium ion irradiation, helium diffusion occurs through three mechanisms.[37] At temperatures below $0.2T_m$, diffusion relies on a displacement mechanism. In this mechanism, vacancies are considered unable to migrate and helium atoms are displaced, which are directly associated with collisions. At temperatures above $0.5T_m$, the dominant mechanism is the vacancy mechanism, which occurs only at temperatures around and above $0.5T_m$, i.e., helium atom jumps from one vacancy to another, in view of this, $D_{He} \sim D_V C_V$. At temperatures between $0.2T_m$ and $0.5T_m$, the main mode of helium diffusion is through a replacement mechanism where helium atoms He_s transform into interstitial sites due to being replaced by interstitial atoms. In this scenario, the helium diffusion coefficient (D_{He}) is proportional to the vacancy diffusion coefficient (D_V), $D_{He} \sim D_V$. Since melting points of four samples irradiated in this study are similar and the irradiation temperature (673 K) is below $0.5T_m$, helium atoms diffuse through replacement mechanism at 673 K, where $D_{He} \sim D_V$, is a valid assumption.

On the one hand, the diffusion of helium may be hindered by the incorporation of Ti atoms. First-principles calculations show that the first nearest neighbor (1n–n) of Ti exhibits a negative value, indicating a strong attraction to the vacancy. Even the second nearest neighbor (2n–n) displays a negative attraction to the vacancy,[38,39] the binding energy of other constituent atoms in the alloy is positive. Therefore, helium atoms in FeCoNiCr$(Ni_3Ti)_{0.1}$ will tend to combine preferentially with oversized Ti to reduce the total free energy of HEAs. A decrease of the effective diffusion coefficient of helium (D_{He}) in the quinary FeCoNiCr$(Ni_3Ti)_{0.1}$ system and further suppression of helium bubbles growth. As a result, helium bubbles in FeCoNiCr alloy revealed a larger diameter of ~ 2.02 nm. On the other hand, the inherent sluggish diffusion property of HEAs also play a critical role in slowing helium diffusion,[40] which prevents the grown helium bubbles from entering into large cavities. Because of the severe lattice distortion in HEAs, at a temperature of 673 K, vacancies are mobile and tend to be annihilated at the phase boundary.[41,42] This leaves the neulei of helium bubbles without enough vacancies to bind and inhibits the growth process of helium bubbles.[6,43] Consequently, helium bubbles in FeCoNiCr$(Ni_3Ti)_{0.1}$ HEAs are all smaller than those in FeCoNiCr as shown in Fig. 6.

4.2. Coherent nanoprecipitates

The experimental outcomes provide insights into the size dependence of coherent nanoprecipitates under irradiation. Overall, helium bubbles were uniformly distributed in the FeCoNiCr$(Ni_3Ti)_{0.1}$ HEAs under experiment (Fig. 6). There were no noticeable differences observed within precipitates or at the γ/γ' interface. It can be concluded that the introduction of γ' precipitates did not change the nucleation mechanism of the helium bubbles, as it remained a homogenous

nucleation process.[44–46] Generally, the interface of a nano-precipitated phase, such as oxide-dispersion-strengthened materials, proves to be an effective site for eliminating point defect.[47–49] This helps prevent the harmful defects from accumulating *in situ*, thereby efficiently enhancing the material's resistance to radiation damage. The chemically disordered complex structure inherent in high-entropy alloys also reduces the mean free path of atoms, increases the probability of point defect recombination, and lowers the vacancy supersaturation concentration.[50–52] This decrease in vacancy flux to the helium bubbles, coupled with inhibited helium atom mobility, leads to a reduction in the growth of the helium bubbles in multiple components and dual-phase HEAs. So that the sizes and density of helium bubbles in the present γ and γ' dual-phase FeCoNiCr$(Ni_3Ti)_{0.1}$ HEAs are smaller than those in single-phase FeCoNiCr.

Simultaneously, the coherent interface serves as a vacancy defect that tends to selectively trap helium atoms,[18,53] resulting in a lower concentration of surviving helium atoms in alloys, hindering the He bubbles from nucleating and the size and density of He bubbles from further decreasing. In the 673-K irradiation experiment, the average size and density of helium bubbles in HEA-16 are smaller than those in HEA-37 and HEA-63, which can be ascribed to the size effect of coherent nanoprecipitates. The stress field of elastic distortion at the heterogeneous coherent interface can trap helium atoms, pinning it so that the nucleation and growth of helium bubbles are suppressed.[42] With immovable phase boundaries, the sink strength of γ' phase interface in HEA-16 approves stronger, so more helium atoms are trapped. Typically, the density of helium bubbles (C_B) is negatively correlated to the atomic diffusion rate of helium atom (D_{He}),[35] while the size of helium bubbles (R_B) is positively correlated to D_{He}:

$$C_B \propto \left[\left(D_{He}^{eff}\right)^{-\beta} P_{He}^{2(\beta-\alpha)} t^{\beta-\alpha}\right]^{1/(3\beta-2\alpha)}, \tag{3}$$

$$R_B \propto \left(D_{He}^{eff} P_{He} t^2\right)^{1/(3\beta-2\alpha)}, \tag{4}$$

where P_{He} is the production rate of He, t is the time of helium bubble evolution, α and β are constants, depending on the state of the helium bubbles. However, it is noteworthy that the HEA-16 sample in this study has the smallest helium bubble size as well as the smallest helium bubble density as shown in Fig. 7, verifies that the varying size of precipitates in high-entropy alloys leads to distinct ability of the phase boundary to trap helium atoms. It is commonly believed that the second phase strengthening principle in mechanical properties is based on the fact that smaller second phase size and more dispersed distribution bring about better strengthening effects.[47] However, studies have shown that the helium atom entrapment capability of the coherent interface exhibits a clear size dependence.[26,27] The variation of size of the heterogeneous coherent γ' phase confirms that the ability to trap helium atoms is different, and contribution to irradiation resistance is also different. It is theorized that there exists an optimum size for radiation resistance which is manifested as 15.80 nm at 673 K. Moreover, the irradiation resistance performance of HEA-37 is not significantly improved compared with that of HEA-63, emphasizing the importance of avoiding excessively oversized precipitates for effective irradiation resistance improvement.

The interface serves as a mechanism to promote vacancies and interstitials (V–I) recombination and stabilize the helium bubbles.[54,55] In this HEA system experiment, the γ/γ' interface demonstrates substantial vacancy sink efficiency. Because the mismatch between the coherent interface and the matrix is very small ($\sim 0.084\%$), an elastic strain field is generated which obstructs the process of defect evolution and facilitates their mutual recombination. The coherency stress drives the defects to move towards the interface, thereby improving helium capture capability.[56] While previous studies introduced precipitates to promote V–I annihilation for defect reduction,[57,58] this work reveals that the heterogeneous coherent interface may inhibit the helium bubble evolution process by pinning helium, thereby improving the irradiation resistance. The $L1_2$-type coherent nanoparticles provide certain sinks for He entrapment and radiation damage elimination, effectively preventing the He bubbles from growing into larger ones and thus providing sustainable resistance to irradiation. Our work suggests that the coherent nanosized interface is also effective to alleviate radiation induced damage in FCC HEAs.

4.3. The E_a for helium bubbles

The diffusion coefficient is temperature dependent and can be well expressed by the Arrhenius equation[59]

$$D = D_0 \exp\left(-\frac{E_a}{kT}\right), \tag{5}$$

where T is the temperature in unit Kelvin, D_0 is the prefactor (diffusion coefficient at infinite temperature), E_a represents the apparent activation energy, and k is the Boltzman constant. Helium bubbles are counted after irradiation at 293 K and subsequent annealing at varying temperatures. The data are then fitted linearly by using Eq. (5), and the fitting results are shown in Fig. 9, where the slopes of the lines indicate the values of apparent activation energy (E_a) for helium bubbles in three HEAs. These values of energy E_a are calculated to be 0.8796 eV, 0.1737 eV, and 0.7009 eV for samples FeCoNiCr, HEA-16, and HEA-63, respectively.

The experimental results of Zell show that the apparent activation energy for pure nickel is equal to 0.45 eV in a temperature range of 523 K–800 K.[60] In addition, the results of Jublot-Leclerc *et al.* showed that the apparent activation energy for 316L SS is 0.39 eV at 723 K–823 K.[61] According to the results of Fu *et al.*,[62] the apparent activation energy of helium bubbles shows a temperature dependence, which is

due to the fact that the stable existence of helium bubbles is influenced not only by the nucleation course of helium atoms, but also by the process of diffusion and growth of He bubbles.

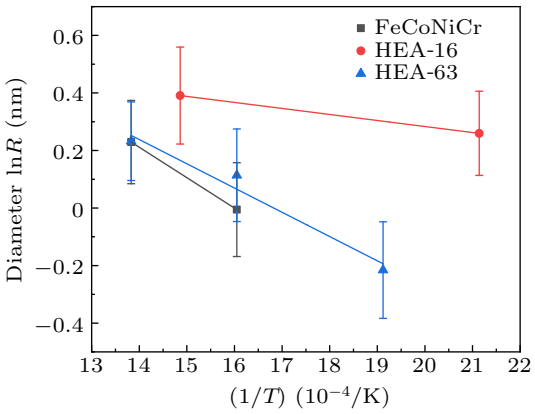


Fig. 9. Results fitted with Arrhenius equation.

During the irradiation experiments, vacancies are mobile at high temperatures of 673 K and are annihilated at phase boundaries, which suppresses the nucleation and growth of helium bubbles.[19,29] The annealing experiment involves irradiation at 273 K followed by heating and annealing in a TEM. When irradiated at room temperature, the vacancies are considered to be immovable, resulting in a large number of surviving vacancies.[5] In the heating and annealing process, helium atoms with a smaller value of apparent activation energy (HEA-16) diffuse faster, bind to vacancies, and promote the growth of helium bubbles. Based on Fig. 9, it appears that the helium bubbles in HEA-16 have a smaller value of apparent activation energy and a faster diffusion rate, resulting in larger bubble size. The apparent activation energy for He bubbles can turm smaller with the introduction of the precipitated phase,[60,63] the conclusion is consistent with our experimental results. When the samples are irradiated at 293 K, the vacancy defects inside the samples are considered to be immovable, resulting in a large number of vacancies surviving, and the nuclei of helium bubbles ($E_a = 0.1737$ eV) which rapidly diffuse in the sample HEA-16 have the opportunity to combine with more vacancies to form helium bubbles after high temperature annealing.

5. Conclusions

In summary, FeCoNiCr$(Ni_3Ti)_{0.1}$ HEAs containing different sizes γ' precipitates and FeCoNiCr alloys are prepared and then they are irradiated with 100-keV helium ions at 293 K and 673 K. The average diameter and density of He bubbles in HEA-16 at 673 K are measured to be 1.5 nm and 0.5×10^{16} m^{-2}, respectively, which are the smallest values. Moreover, we identify an interfacial interaction with helium that can improve the radiation resistance of FeCoNiCr$(Ni_3Ti)_{0.1}$ HEAs as compared with that of single-phase HEAs at 673 K. Annealing experiments conducted after 293-K irradiation indicate that the FeCoNiCr$(Ni_3Ti)_{0.1}$ HEAs exhibit smaller values of apparent activation energy for helium bubbles, resulting in larger helium bubble sizes. Our study suggests the effectiveness of a nanoscale heterogeneous coherent γ/γ' interface in mitigating irradiation induced damages. These findings provide some ideas for designing advanced $L1_2$-strengthened HEAs with superior radiation tolerance in future reactors.

Acknowledgements

Project support provided by the National Natural Science Foundation of China (Grant No. 12075200) and the National Key Research and Development Program of China (Grant No. 2022YFB3706004).

References

[1] Zinkle S J and Was G S 2013 *Acta Materialia* **61** 735
[2] Zinkle S J, Terrani K A and Snead L L 2016 *Current Opinion in Solid State & Materials Science* **20** 401
[3] Zinkle S J and Busby J T 2009 *Mater. Today* **12** 12
[4] Barr C M, *et al*. 2014 *Acta Materialia* **67** 145
[5] Kumar N, Li C, Leonard K J, Bei H and Zinkle S J 2016 *Acta Materialia* **113** 230
[6] Kumar N, *et al*. 2016 *Acta Materialia* **113** 230
[7] Li S H, Li J T and Han W Z 2019 *Materials* **12** 071036
[8] Chen D, Zhao S J, Sun J R, Tai P F, Sheng Y B, Zhao Y L, Yeli G, Lin W T, Liu S F, Kai W and Kai J J 2019 *J. Nucl. Mater.* **526** 151747
[9] Cheng T, Wei G, Jiang S M, Zhang J, Wang Y Q, Liu P, Hong M Q, Guo E K, Zhong F, Cai G X, Jiang C Z and Ren F 2023 *Acta Materialia* **248** 118765
[10] Tsai M H and Yeh J W 2014 *Mater. Res. Lett.* **2** 107
[11] Miracle D B and Senkov O N 2017 *Acta Materialia* **122** 448
[12] Cantor B 2014 *Entropy* **16** 4749
[13] George E P, Raabe D and Ritchie R O 2019 *Nat. Rev. Mater.* **4** 515
[14] Lu C Y, Niu L L, Chen N J, Jin K, Yang T N, Xiu P Y, Zhang Y W, Gao F, Bei H B, Shi S, He M R, Robertson I M, Weber W J and Wang L M 2016 *Nat. Commun* **7** 13564
[15] Zhang Y 2023 *High-Entropy Materials: Advances and Applications* (Boca Raton: CRC Press)
[16] Ming K S, Bi X F and Wang J 2018 *Int. J. Plasticity* **100** 177
[17] Ahlgren T and Bukonte L 2017 *J. Nucl. Mater.* **496** 66
[18] Vattré A, Jourdan T, Ding H, Marinica M C and Demkowicz M J 2016 *Nat. Commun.* **7** 10424
[19] Zheng Y, Lu W, Qian F, Jia N, Dou Y, He X, Yang W, Wang J, Xue Y and Jin K 2021 *J. Nucl. Mater.* **549** 152889
[20] Zhao S J and Osetsky Y 2021 *Acta Materialia* **207** 116704
[21] Kalita D, Józwik I, Kurpaska L, Zhang Y, Mulewska K, Chrominski W, O'Connell J, Ge Y, Boldman W L, Rack P D, Wang Y, Weber W J and Jagielski J 2023 *Nucl. Mater. Energy* **37** 101513
[22] Shen S K, Hao L Y, Liu X, Wang Y F, Li Y X, Zhang J and Fu E G 2023 *Acta Materialia* **261** 119404
[23] Wang K, Yan Y G, Xiong Y X, Zhao S J, Chen D and Woller K B 2024 *J. Nucl. Mater.* **588** 154761
[24] Lin W T, *et al*. 2022 *J. Mater. Sci. Technol.* **101** 226
[25] Chen D, Zhao S J, Sun J R, Tai P F, Sheng Y B, Yeli G, Zhao Y L, Liu S F, Lin W T, Kai W and Kai J J 2020 *J. Nucl. Mater.* **542** 152458
[26] Chen Y X, *et al*. 2015 *J. Mater. Res.* **30** 1300
[27] Fu E G, *et al*. 2010 *J. Nucl. Mater.* **407** 178
[28] Cao P P, Wang H, He J Y, Xu C, Jiang S H, Du J L, Cao X Z, Fu E G and Lu Z P 2021 *J. Alloys Compd.* **859** 158291
[29] Zhaoa Y L, *et al*. 2023 *J. Mater. Sci. Technol.* **143** 169
[30] Tang B, *et al*. 2014 *Mater. Trans.* **55** 410
[31] Yao B, *et al*. 2012 *J. Electron Microscopy* **61** 393
[32] Yen S Y, Murakami H and Lin S K 2023 *J. Alloys Compd.* **952** 170027

[33] He H H, Lin Z W, Jiang S M, Hu X T, Zhang J and Huang Z J 2021 *Materials* **14** 3727
[34] Zhu R, Zhou Q, Shi L, *et al*. 2021 *Chin. Phys. B* **30** 086102
[35] Trinkaus H and Singh B N 2003 *J. Nucl. Mater.* **323** 229
[36] Harrison R W, Greaves G, Le H, Bei H, Zhang Y and Donnelly S E 2019 *Current Opinion in Solid State & Mater. Sci.* **23** 100762
[37] Chernikov V N, Trinkaus H and Ullmaier H 1997 *J. Nucl. Mater.* **250** 103
[38] Fu C C and Willaime F 2005 *Phys. Rev. B* **72** 064117
[39] Ortiz C J, Caturla M J, Fu C C and Willaime F 2007 *Phys. Rev. B* **75** 100102
[40] Tong Y, *et al*. 2019 *Acta Materialia* **165** 228
[41] Parkin C, Chen W Y, Li M M, Sridharan K and Couet A 2024 *J. Nucl. Mater.* **589** 154827
[42] Wang Q Q, Kong X G, Yu Y, Xin T Y, Pan R J and Wu L 2023 *J. Nucl. Mater.* **587** 154706
[43] [43] Wang Y B, Li S Y, Chen F D, Yang K, Ge G J, Tang X B, Fan M Y and Huang P 2023 *J. Alloys Compd.* **958** 170373
[44] Bergstrom Z J, Perez D and Martinez E 2021 *J. Nucl. Mater.* **557** 153306
[45] Jelea A 2018 *Nucl. Instrum. Methods Phys. Res. B* **425** 50
[46] Schaldach C M and Wolfer W G 2002 *Kinetics of helium bubble formation in nuclear and structural materials*, in 21*st Int. Symposium on Effects of Radiation on Materials* 2002, Tucson, AZ 1447 479
[47] Hsiung L L, Fluss M J, Tumey S J, Choi B W, Serruys Y, Willaime F and Kimura A 2010 *Phys. Rev. B* **82** 184103
[48] Schäublin R, *et al*. 2006 *J. Nucl. Mater.* **351** 247
[49] Ukai S and Fujiwara M 2002 *J. Nucl. Mater.* **307** 749
[50] Gao X F, Liu T, Zhang X F, Fang H Z, Qin G and Chen R R 2022 *J. Alloys Compd.* **918** 165584
[51] Jiang K, Ren T F, Shan G B, Ye T, Chen L Y, Wang C X, Zhao F, Li J G and Suo T 2020 *Mater. Sci. Eng. A* **797** 140125
[52] Lu W J, *et al*. 2020 *Acta Materialia* **185** 218
[53] Yang W F, Pang J Y, Zheng S J, Wang J, Zhang X H and Ma X L 2019 *Materials* **12** 2639
[54] Pu G, Lin L W, Ren D, Gan K F, Liu B, Ye Z B, Wang Y H, Zhang K, Li Z M and Liu B 2022 *J. Nucl. Mater.* **566** 153734
[55] Shun T T, Hung C H and Lee C F 2010 *J. Alloys Compd.* **493** 105
[56] Liu L Y, Zhang Y, Han J H, Wang X Y, Jiang W Q, Liu C T, Zhang Z W and Liaw P K 2021 *Adv. Sci.* **8** 2100870
[57] Zhang H Z, Zhu Z B, Huang H F, He T, Yan H W, Zhang Y A, Lu Y P, Wang T M and Li T N G 2023 *Intermetallics* **157** 107873
[58] Wang Y F, Chen H Q, Sun B R, Li X W, Meng Q N, Wu Z F, Hao L Y, Du J L, Liu X, Shen T D, Zhang J, Li J and Fu E G 2023 *Mater. Today Commun.* **36** 106897
[59] Wang Y Z and Wang Y J 2022 *Acta Materialia* **224** 117527
[60] Zell V, Schroeder H and Trinkaus H 1994 *J. Nucl. Mater.* **212** 358
[61] Jublot-Leclerc S, *et al*. 2015 *J. Nucl. Mater.* **466** 646
[62] Fu C L, Li J J, Bai J J, Lei Q T, Liu R D and Lin J 2022 *J. Nucl. Mater.* **562** 153609
[63] Sun G A, *et al*. 2014 *Thin Solid Films* **558** 125
[64] Yan Z F, *et al*. 2018 *J. Nucl. Mater.* **505** 200